Available online at www.sciencedirect.com
ScienceDirect
International Journal of Thermal Sciences 46 (2007) 1219–1231
International Journal of Thermal Sciences
www.elsevier.com/locate/ijts

Study of buoyancy-induced flows subjected to partially heated sources on the left and bottom walls in a square enclosure

Tzong-Huei Chen *, Li-Yueh Chen

Department of Mechanical Engineering, Dahan Institute of Technology, No. 1, Sujen Street, Dahan, Sincheng, Hualien 97145, Taiwan, ROC

Received 19 July 2005; received in revised form 27 November 2006; accepted 27 November 2006

Available online 24 January 2007

Abstract

In this paper, numerical simulations of laminar, steady, two-dimensional natural convection flows in a square enclosure with discrete heat sources on the left and bottom walls are presented using a finite-volume method. Two different orientated wall boundary conditions are designed to investigate the natural convection features. The computational results are expressed in the form of streamlines and isothermal lines for Rayleigh numbers ranging from 10^2 to 10^7 in the cavity. In the course of study, a combination of third-order and exponential interpolating profile based on the convective boundedness criterion is proposed and tested against the partially heated cavity flow up to the highest Rayleigh number 10^7. The effects of thermal strength and heating length on the hydrodynamic and thermal fields inside the enclosure are also presented. Numerical results indicate that the average Nusselt number increases as Rayleigh number increases for both cases. Moreover, it is seen that the effect of the heat transfer rate due to the heating strength on the left wall is different from the one on the bottom. For the heater size effect, it is observed that by increasing the length of heat source segment, the heat transfer rate is gradually increased for both cases.

Keywords: Natural convection; Discrete heat sources; Convective boundedness criterion

1. Introduction

Natural convection in a two-dimensional square cavity with differentially heated walls has drawn considerable attention in a number of important engineering applications such as electronic equipment cooling, solar energy collectors, and nuclear reactors. These discrete heaters may be placed either on horizontal wall or vertical wall, representing certain interesting features of flow field and the heat transfer rate in a range of Rayleigh numbers. Chu et al. [1] is the pioneer to study the effects of heater size, location, and boundary conditions on the left wall of the rectangular buoyant cavity both experimentally and numerically. They focused on the understanding of the thermal boundary layer developing along the wall, the rate of heat transfer, and the recirculation patterns in the core region. General agreement between experiment and numerical result was found from their investigation. Ahmed and Yovanovich [2] examined a square enclosure with a heat source located in the center of one vertical side for Rayleigh number from 0 to 10^6. The effect of the heat size normalized by the cavity height ranging from 0.25 to 1.0 was thoroughly discussed. Correlation equations for Nusselt number, Rayleigh number, and heat size ratio were proposed. This represents a consideration of thermal effects when a number of electronic components were packed into a tiny chip. Bae and Hyun [6] carried out detailed numerical study on the heat transfer induced by buoyancy effect for a tall rectangular cavity with three discrete heat sources on the vertical wall. The case simulated by Bae is comparable to the practical design of electronic devices. Geometrical conditions related to the heater arrangement are specified with fixed sizes throughout the entire study. Rayleigh number effect and transient stage of natural convection are discussed.

Aydin and Yang [3] investigated a buoyancy-induced cavity having a centrally thermal strength located on the bottom wall and symmetrically cooled sidewalls. By considering the effects of the Rayleigh number and dimensionless heat source length, the counter-rotating cells inside the cavity were found. It is concluded by them that increasing heating length or increas-

* Corresponding author.
E-mail address: thchen@ms01.dahan.edu.tw (T.-H. Chen).

1290-0729/$ – see front matter
doi:10.1016/j.ijthermalsci.2006.11.021

Nomenclature

A	model constant ($= a/b$)		
a, b	TOE scheme model constants		
C_p	heat capacity	$\mathrm{J\,kg^{-1}\,K^{-1}}$	
L_1	heating length on the left wall	m	
L_2	heating length on the bottom wall	m	
L	length scale of the square cavity	m	
ℓ_1	dimensionless heating length on the left wall		
ℓ_2	dimensionless heating length on the bottom wall		
$\overline{Nu}$	average Nusselt number along the right wall		
P	reduced pressure or space between two heat sources	Pa or m	
p	dimensionless insulated length		
Pr	Prandtl number		
Ra	Rayleigh number, $\frac{\varrho g\beta \Delta T L^3 C_p}{k\mu}$		
Re	Reynolds number, $\varrho U L/\mu$		
T_0	reference temperature	K	
T_C	right cold temperature	K	
T_{H1}	left hot temperature	K	
T_{H2}	bottom hot temperature	K	
ΔT	temperature difference $T_{H1} - T_C + T_{H2} - T_C$	K	
u, v	velocity components in x, y directions	$\mathrm{m\,s^{-1}}$	

Greek symbols

β	thermal expansion coefficient	$\mathrm{K^{-1}}$
ϕ	dependent variable	
$\hat{\phi}$	non-dimensional variable	
κ	thermal conductivity	$\mathrm{W\,m^{-1}\,K^{-1}}$
μ	viscosity	$\mathrm{Pa\,s^{-1}}$
ρ	density	$\mathrm{kg\,m^{-3}}$
θ_1	dimensionless temperature, $(T_1 - T_C)/\Delta T$	
θ_2	dimensionless temperature, $(T_2 - T_C)/\Delta T$	
ξ_1	TOE scheme model constant	
ξ_2	TOE scheme model constant	

ing Rayleigh number resulted in an increased heat transfer rate. Hasnaoui et al. [4] studied an enclosed cavity with localized heating from below, stressing on the effects of the dimensionless heat length and position of the heat source, and Rayleigh number ($Ra = 0$ to 5×10^6) on flow and temperature fields. Deng et al. [5] investigated natural convection in rectangular enclosures by implementing two constant heat flux sources on bottom wall. They were interested in the heating strength and the space between two heat sources at fixed Rayleigh number of 10^5. The upward flow pattern in the center region was observed at the non-dimensional separate distance of the heat sources less than one while the downward flow pattern was found at the non-dimensional distance greater than one.

It is noticed that these aforementioned studies are emphasized on the discussion of discrete heat sources on one wall only. However, there are some engineering applications imposed with simultaneous heating or cooling on the side and bottom walls. Deng et al. [7] employed a combined temperature scale to numerically study the heaters on the left and bottom walls in rectangular enclosures for Rayleigh number range 10^3–10^6. The parameters of their investigation include the Rayleigh number, the heater strength, and heater size. The numerical results regarding the effects of heating strength and heating length presented on thermal and flow fields were presented at Rayleigh number of 10^5. It is observed that these studies are limited to a single heat source on two walls, respectively. In practice, an enclosure flow over non-uniform heating walls is much more realistic. For example, the electronic components representing certain amount of heat sources were mounted on electric circuit boards which can be configured in the vertical and horizontal directions simultaneously on the equipment frame. With discrete heat sources on the side and bottom walls simultaneously, it will be interesting to see more complex interaction between the buoyancy induced flow and heat transfer rate inside the cavity. The first objective of this study is to examine the flow and temperature fields in consideration of more complex enclosure wall conditions with differentially heated sources on the upright and floor walls.

De Felice et al. [8] studied highly convective transport problems including single-step flow, lid-driven cavity flow, and laminar natural convection in a differentially heated square cavity. They found oscillating solutions at $Ra = 10^7$ in the cavity. In our study, we use a high-order QUICK scheme and have experienced the numerical oscillating solution at $Ra = 10^7$ for the natural convection in the cavity. The high-order numerical scheme implies high accuracy of numerical prediction. However, the high-order scheme sometimes can result in a numerical instability. To ensure a convergent numerical solution of the natural convection subjected to discrete heat sources, it is necessary to recognize the high Rayleigh number problem using QUICK scheme. The second objective here is to solve the numerical difficulty of QUICK scheme at high Rayleigh number. A convection boundedness criterion scheme called TOE is proposed and tested against some laminar flows.

In the light of the above observations, two different test cases considered in the square enclosure are designed to analyze the natural convection flow. In the first case, the window cavity is partially heated on the left upper wall and two discrete heat sources are placed on the bottom wall. The unspecified regions on the left and bottom walls are insulated. The right wall is maintained at a cold temperature and the top wall is well insulated as shown in the Fig. 1. Note that in the figure the space between two heat sources on the bottom is specified by P distance. This is referred as Case A. In the second one, two discrete heat sources are located on the left vertical wall and one thermal source is placed along the left part of the bottom wall as shown in Fig. 1. This is referred as Case B. The presence of heaters on the vertical and horizontal wall simultaneously may cause the interaction between hydrodynamic and thermal fields inside the cavity for different configurations, Cases A and B. In

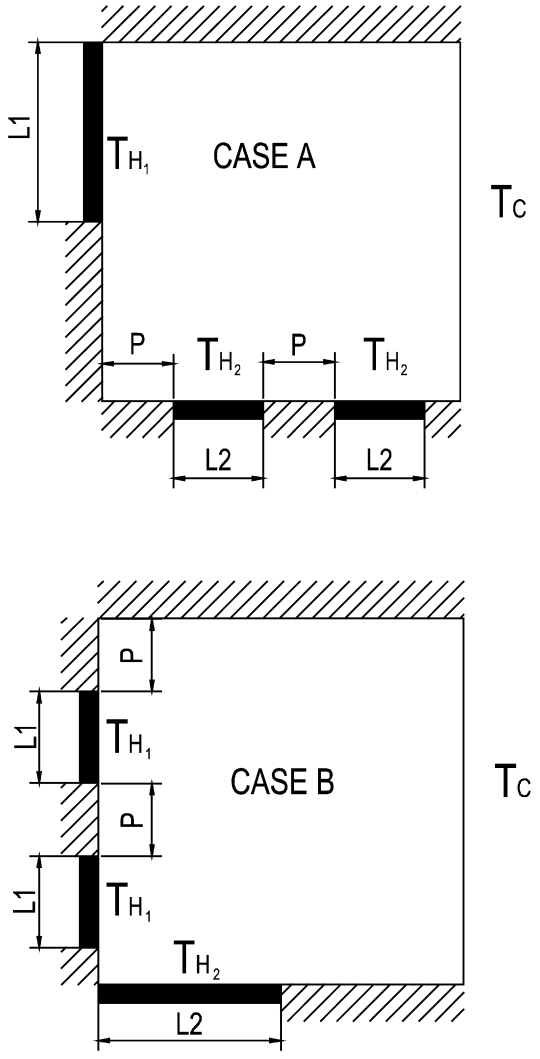

Fig. 1. The described Cases A and B for natural convection study.

view of these cases, it is inquiring to observe the temperature fields and flow patterns inside the cavity and to check the heat transfer rate.

2. Mathematical formulation

The governing equations for the laminar, steady, two-dimensional flow using the Boussinesq approximation can be written as follows

$$\frac{\partial(\varrho u)}{\partial x}+\frac{\partial(\varrho v)}{\partial y}=0 \tag{1}$$

$$\varrho u\frac{\partial u}{\partial x}+\varrho v\frac{\partial u}{\partial y}=\frac{\partial}{\partial x}\left[\mu\frac{\partial u}{\partial x}\right]+\frac{\partial}{\partial y}\left[\mu\frac{\partial u}{\partial y}\right]-\frac{\partial P}{\partial x} \tag{2}$$

$$\varrho u\frac{\partial v}{\partial x}+\varrho v\frac{\partial v}{\partial y}=\frac{\partial}{\partial x}\left[\mu\frac{\partial v}{\partial x}\right]+\frac{\partial}{\partial y}\left[\mu\frac{\partial v}{\partial y}\right]-\frac{\partial P}{\partial y}+\varrho g\beta(T-T_0) \tag{3}$$

$$\varrho u\frac{\partial T}{\partial x}+\varrho v\frac{\partial T}{\partial y}=\frac{\partial}{\partial x}\left[\frac{\mu}{Pr}\frac{\partial T}{\partial x}\right]+\frac{\partial}{\partial y}\left[\frac{\mu}{Pr}\frac{\partial T}{\partial y}\right] \tag{4}$$

where u and v are velocities, T is the temperature, T_0 is the referenced temperature, P is the reduced pressure, μ is the fluid viscosity, Pr is the Prandtl number, and β is the thermal expansion coefficient. To reach high accuracy of numerical predictions in our current computations, the convection term is discretized using a high-order QUICK scheme coupled with a deferred correction method. The pressure–velocity coupled equation is solved by SIMPLE algorithm. The momentum and temperature equations were then solved using the tri-diagonal matrix algorithm with a sweep in each direction. Moreover, the computational results are considered to be converged if the dependent variables for all grid points satisfy the following criterion

$$\sum_{u,v,T}\max\left|\frac{\phi^{\text{new}}-\phi^{\text{old}}}{\phi^{\text{new}}}\right|\leqslant 10^{-5} \tag{5}$$

However, the high-order convective scheme is often connected to an unphysical oscillation or under/over-shoot phenomena in regions of steep gradients. This high-order scheme suffers from the so-called boundedness problem described by Leonard [9]. Fundamentally, monotonic constraints or bounded schemes for the high-order scheme must be enforced to annihilate the numerical dispersion. In an effort to conquer this numerical difficulty, the composite flux scheme based on the normalized variable formulation (NVF) proposed by Leonard [9] is considered in our study. With this in advance, a new scheme based on NVF to eliminate the numerical scatter is thus proposed. It is described in the next section.

3. Proposed TOE scheme

Consider the uniformly-spaced control volumes centered at $\mathrm{i}-2$, $\mathrm{i}-1$, and i. The dependent variable following Leonard's NVF [9] at the interface between $\mathrm{i}-1$ and i can be normalized as

$$\hat{\phi}_{\mathrm{i}-1/2}=\frac{\phi_{\mathrm{i}-1/2}-\phi_{\mathrm{i}-2}}{\phi_{\mathrm{i}}-\phi_{\mathrm{i}-2}} \tag{6}$$

where $\mathrm{i}-1/2$ represents the right surface of the control volume $\mathrm{i}-1$. As pointed out by Gaskell and Lau [10], if an implicit steady-state flow calculation is sought in NVF, the normalized variable in Eq. (6) should satisfy the convective boundedness criterion (CBC) in the shaded region as shown in Fig. 2. Leonard [9] mentioned that for uniform grids, the QUICK scheme was bounded only in the interval $1/4\leqslant\hat{\phi}_{\mathrm{i}-1}\leqslant 3/4$. However, the remaining intervals $0\leqslant\hat{\phi}_{\mathrm{i}-1}\leqslant 1/4$ and $3/4\leqslant\hat{\phi}_{\mathrm{i}-1}\leqslant 1$, are unbounded. In order to resolve the unbound problem, we propose a new non-linear relationship between $\hat{\phi}_{\mathrm{i}-1/2}$ and $\hat{\phi}_{\mathrm{i}-1}$ as

$$\frac{d\hat{\phi}_{\mathrm{i}-1/2}}{d\hat{\phi}_{\mathrm{i}-1}}=a\hat{\phi}_{\mathrm{i}-1/2}+b \tag{7}$$

where a and b are model constraints and they are required to be determined in these two intervals. Note that the proposed relationship between $\hat{\phi}_{\mathrm{i}-1/2}$ and $\hat{\phi}_{\mathrm{i}-1}$ is someway arbitrary, emphasizing particularly on the monotonic relationship between $\hat{\phi}_{\mathrm{i}-1/2}$ and $\hat{\phi}_{\mathrm{i}-1}$. The task is to determine model constraints a

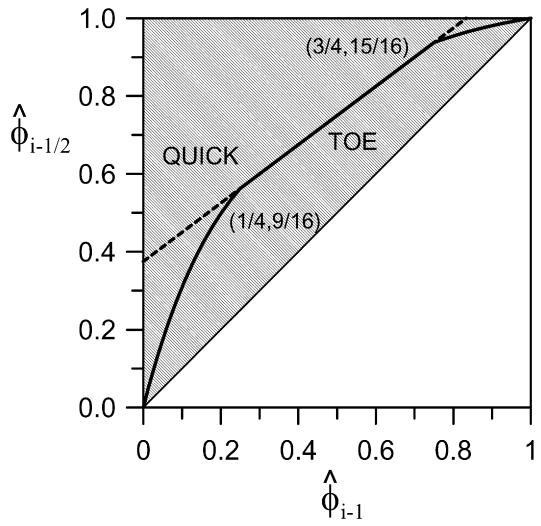

Fig. 2. Presented TOE scheme in CBC diagram.

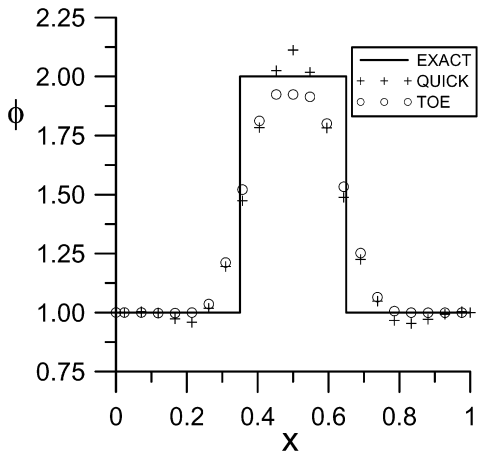

Fig. 3. Predicted box-shape profiles with grid size of 21 × 21 points.

and b in these two intervals. For the sake of simplicity, if an intermediate value $\hat{\phi}_{i-1} = 1/8$ in the interval $0 \leqslant \hat{\phi}_{i-1} \leqslant 1/4$, which is just half distance of this interval, is employed, we will have a corresponding value of $\hat{\phi}_{i-1/2}$. For convenience, this value is designated as ξ_1 in our notation. For a similar selection of an intermediate value $\hat{\phi}_{i-1} = 7/8$, the corresponding $\hat{\phi}_{i-1/2}$ is set to ξ_2. Then, the solutions of Eq. (7) in these two intervals can be obtained as:

In the interval $0 \leqslant \hat{\phi}_{i-1} \leqslant 1/4$,

$$\hat{\phi}_{i-1/2} = A\left(e^{-a\hat{\phi}_{i-1}} - 1\right) \tag{8}$$

where a and A $(= a/b)$ are

$$a = -8\ln\frac{9-16\xi_1}{16\xi_1}, \qquad A = \frac{9}{16}\frac{1}{(\frac{9-16\xi_1}{16\xi_1})^2 - 1}$$

$$\frac{2}{16} \leqslant \xi_1 \leqslant \frac{9}{16} \tag{9}$$

In the interval $3/4 \leqslant \hat{\phi}_{i-1} \leqslant 1$,

$$\hat{\phi}_{i-1/2} = A\left[e^{-a(1-\hat{\phi}_{i-1})} - 1\right] \tag{10}$$

where a and A are

$$a = -8\ln\frac{1}{16(1-\xi_2)}$$

$$A = -\frac{1}{16}\frac{1}{([16(1-\xi_2)]^{-1} - 1)^2 - 1}$$

$$\frac{15}{16} \leqslant \xi_2 \leqslant 1 \tag{11}$$

Note that ξ_1 is confined in the interval, (2/16, 9/16) and ξ_2 is confined in the interval (15/16, 1). Consequently, the entire model becomes dependent on ξ_1 and ξ_2 only in these two intervals. The strategy here is to determine the value of ξ_1 first. Let us consider the normalized $\hat{\phi}_{i-1/2}$ profile as an exponential function of x and assume the exponential function passes through points $(0, 0)$, $(1/2, 1/8)$, and $(1, 1)$ in a unity diagram. Then, the exponential function can be solved as

$$\hat{\phi}_{i-1/2} = \frac{1}{48}\left(e^{2\ln 7\cdot x} - 1\right) \tag{12}$$

It is noticeable that at $x = 0$, $x = 1/2$, and $x = 1$, the corresponding values $\hat{\phi}$ can be interpreted as $\hat{\phi}_{i-2}$, $\hat{\phi}_{i-1}$, and $\hat{\phi}_i$, subsequently. Therefore, at $x = 3/4$, the corresponding $\hat{\phi}_{x=3/4}$ can be viewed as $\hat{\phi}_{i-1/2}$ in the assumed exponential profile. If $x = 3/4$ is substituted into Eq. (12), $\hat{\phi}_{x=3/4} = 0.365005374$. This result makes it applicable to use $\xi_1 = 0.365005374$ corresponding to $\hat{\phi}_{i-1/2}$ as the model determination.

Next, determination of ξ_2 is considered. From our computational experiments, the effect of ξ_2 in the second interval on the numerical results is not so sensitive in this small interval that we simply choose $\xi_2 = 92/96$ for no particular reason. Since this approach is based on a combination of third-order and exponential interpolating profile, it is called TOE scheme. The proposed scheme is shown in Fig. 2. Numerical tests of TOE scheme are presented in the next section.

4. Numerical tests of TOE scheme

The first problem tested for the new high-order TOE scheme is related to the pure convection problem of a box-shaped profile in an oblique velocity field [9] in a square domain. The computational area is described by uniform mesh size of 21 × 21 points. The numerical result is shown in Fig. 3. In Fig. 3, the present TOE model shows no over/under-shoot in the box-shaped region while the QUICK scheme exhibits the scatter phenomena in the stiff region. As mesh size is further refined, 41 × 41 points, similar results were observed, which is not shown in this paper. Further validation of the current computer code is to compare the numerical results of natural convection in the cavity with those obtained from literature in which the average Nusselt number along the cold wall is defined as

$$\overline{Nu} = \frac{1}{\mathsf{L}}\int_0^{\mathsf{L}} \frac{\partial\theta}{\partial n}\, d\ell \tag{13}$$

where θ is the non-dimensional temperature, n is the normal direction to the wall, and the non-dimensional length L is equal to 1. The present TOE scheme results in a average Nusselt number of 8.840 in comparison with 8.80 of De Vahl Davis [11] for 256 × 256 grid points at $Ra = 10^6$. At $Ra = 10^7$, numerical

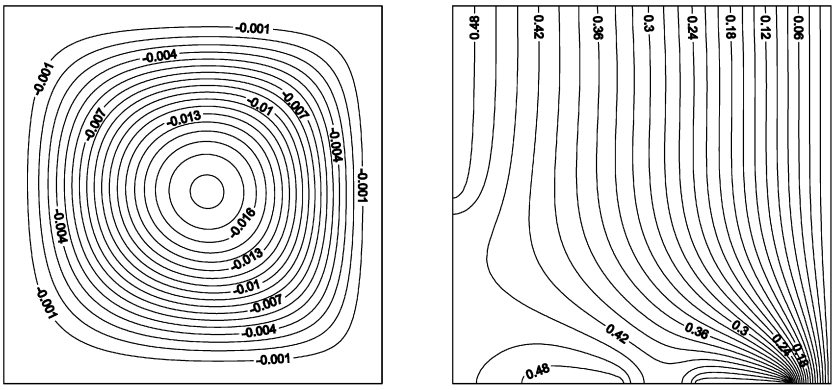

(a) $Ra=10^3$

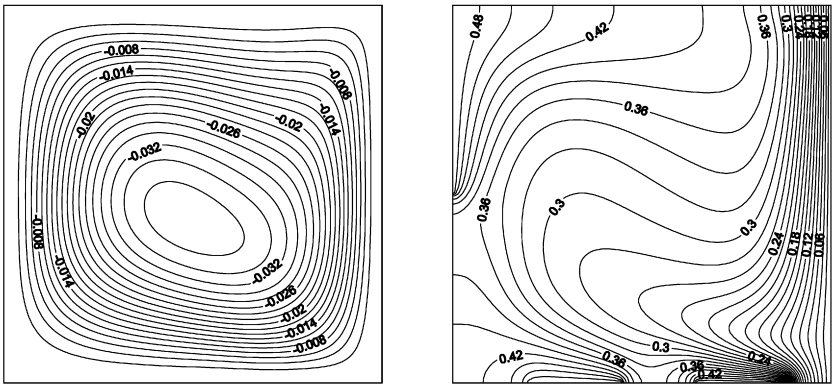

(b) $Ra=10^5$

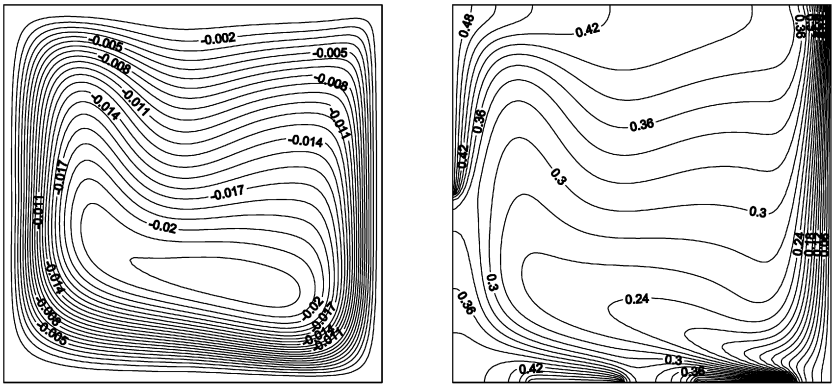

(c) $Ra=10^6$

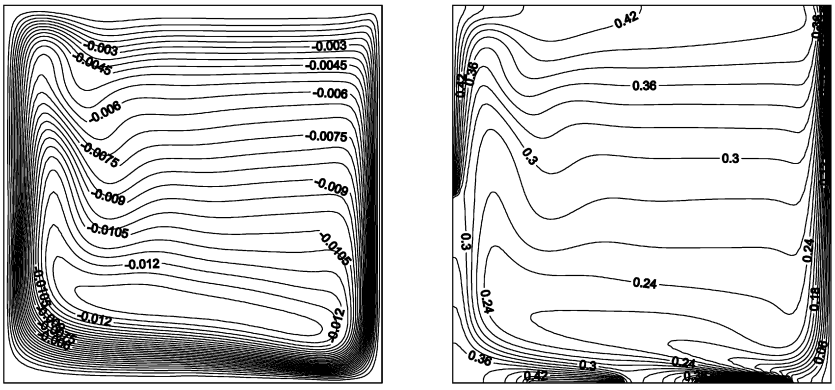

(d) $Ra=10^7$

Fig. 4. The streamlines and isothermal lines for different Rayleigh numbers from (a) to (d) in Case A.

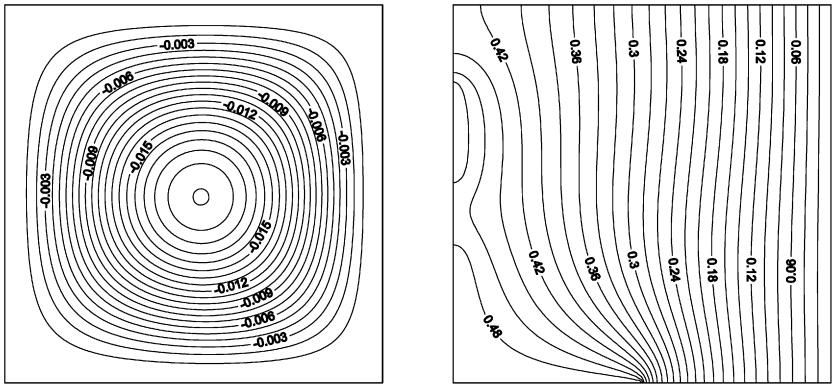

(a) $Ra=10^3$

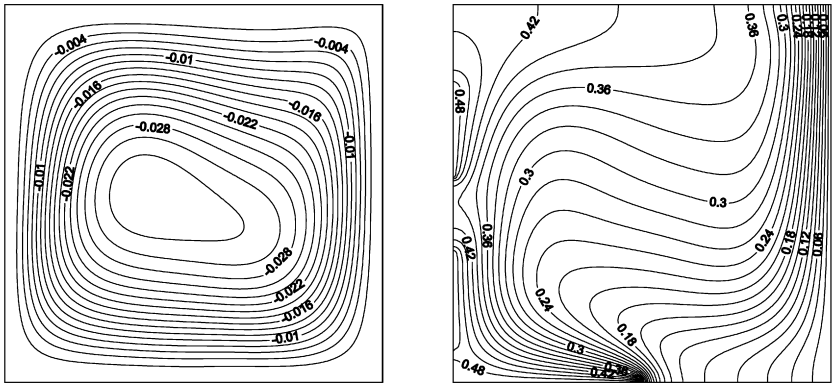

(b) $Ra=10^5$

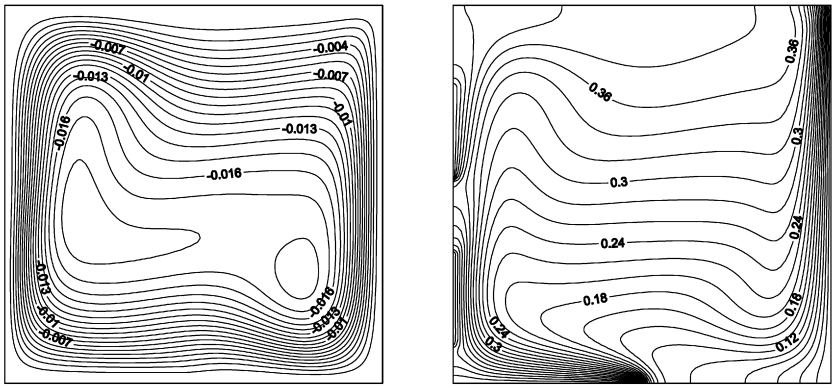

(c) $Ra=10^6$

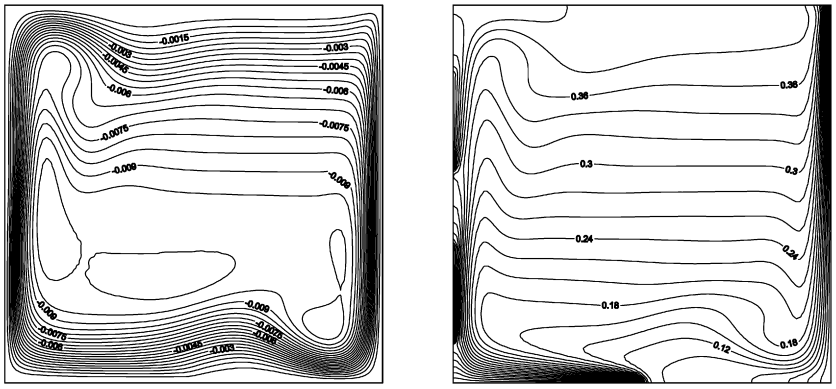

(d) $Ra=10^7$

Fig. 5. The streamlines and isothermal lines for different Rayleigh numbers from (a) to (d) in Case B.

tests of different mesh sizes are conducted. The QUICK scheme leads to an oscillating numerical solution, but the present TOE scheme can result in a convergent solution. Moreover, when the TOE scheme with 81×81 grid points was used to simulate the discrete heat source cavity flow described by Deng et al. [5] at $Ra = 10^5$, the TOE scheme predicts an average Nusselt number of 1.921 compared to 1.924. The accuracy of the numerical results herein was ensured by our computational tests.

5. Results and discussion

For the present study of natural convection flows in the square cavity for Cases A and B, a group of non-dimensional quantities is defined as

$$\ell_1 = \frac{\mathsf{L}_1}{\mathsf{L}}, \qquad \ell_2 = \frac{\mathsf{L}_2}{\mathsf{L}}$$
$$\theta_1 = \frac{T_{H1} - T_C}{\Delta T}, \qquad \theta_2 = \frac{T_{H2} - T_C}{\Delta T}$$
$$Ra = \frac{\varrho g \beta \Delta T L^3 C_p}{k\mu} \tag{14}$$

where $\Delta T = T_{H1} - T_C + T_{H2} - T_C$ and L is the cavity size. Grid independence tests were conducted by using different grid sizes of 81×81, 121×121, and 161×161 points for Case A at $Ra = 10^7$. It is found that the average Nusselt number using 81×81 points compared with that obtained using 161×161 points gives approximate 3% difference while the difference performed by 121×121 points is only 0.3%. Based on these observations, a uniform grid of 121×121 points was used throughout the rest of numerical calculations in this study.

5.1. Effect of Rayleigh number

Computations were carried out at conditions of $p = \mathsf{P}/\mathsf{L} = 0.2$, $\theta_1 = 0.5$, $\theta_2 = 0.5$, and fixed heating lengths, $\ell_1 = 0.5$ and $\ell_2 = 0.25$ in Case A, and $\ell_1 = 0.25$ and $\ell_2 = 0.5$ in Case B. The simulated Rayleigh number is varied from 10^2 to 10^7. Figs. 4 and 5 show the typical results of streamlines and isothermal lines plotted for $Ra = 10^3$, 10^5, 10^6 and 10^7 for Cases A and B. At $Ra = 10^3$, the heat transfer is mainly controlled by conduction as seen the nearly undistorted isothermal lines for both Cases A and B. Moreover, in Case A, the severe temperature gradient occurred at right lower corner elucidates a better heat transfer rate than Case B. At $Ra = 10^5$, the intensity of the convection becomes stronger, which implies that the convection heat transfer begins dominating the thermal flow field in the cavity. As the Rayleigh number becomes large ($Ra = 10^6$), the visualized flow patterns reveal that the fluid rises to left hot wall and then descends down to right cold wall. At the highest $Ra = 10^7$ considered, the crowded streamlines and isothermal lines indicate that the hydrodynamic and thermal boundary layers have been developed along the heated wall and cold wall, respectively, reflecting rigorous heat transfer rate occurred. Distribution of average Nusselt number along the right cold wall as a function of Ra for Cases A and B is shown in Fig. 6. Variation of average Nusselt number is almost unchanged up to $Ra = 10^3$, and then drastically increases with increasing Rayleigh number for both cases. However, Case A shows larger average Nusselt number than Case B as discussed previously. This trend is consistently observed with the increasing Rayleigh number.

5.2. Effect of thermal strength

In order to analyze the thermal strength of the heat sources on the walls affecting the cavity field, the combined temperature scales for left and bottom walls are expressed as $\theta_1 + \theta_2 = 1$ in this study. The temperature scale is designed to allow the increase of the heat strength on the sidewall (θ_1) from 0 to 1 and the decrease of the heat strength on the bottom wall (θ_2) from 1 to 0. The heater sizes are fixed as described in the previous section and the Rayleigh number is varied from 10^2 to 10^7. Figs. 7(a)–(d) and 8(a)–(d) display the streamlines and isothermal lines at $Ra = 10^7$ with different heating strength θ_1s for Cases A and B. Figs. 9(a) and 9(b) show the effects of the increase of heating strength θ_1 on heat transfer rates for different Rayleigh numbers ranging from $Ra = 10^2$–10^7 for Cases A and B. A close inspection of Figs. 9(a) and 9(b) reveals that the effect of the heat transfer rate due to the heating strength on the left wall is different from the one on the bottom. This suggests that a comprehensive examination of the thermal and fluid fields is necessary in order to figure out the causes of different heat transfer rates.

It is interesting to find out that at $\theta_1 = 0$ two counter-rotating cells are observed for both of Cases A and B at $Ra = 10^7$. In Case A, two heat sources on floor deliver heat into the upper left and right cold walls, leading to an asymmetric flow pattern owing to the laterally half insulated situation. There are other cells appearing inside the core region. These multi-cells are not observed for Rayleigh numbers below 10^6 (not shown in the figures). As a result, it is clear that heat transfer rate at $Ra = 10^7$ is greater than that of $Ra = 10^6$. In Case B, two rolls stem from the vertical wall. Note that the single heat source on the bottom conveys most heat into the left cold wall due to a large temperature difference as seen by the cluster constant temperature lines close to the left corner. As a result, it exhibits a higher

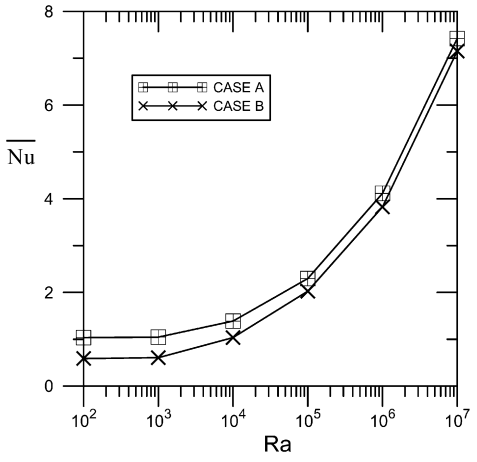

Fig. 6. The effect of Ra numbers on average Nusselt numbers for Cases A and B.

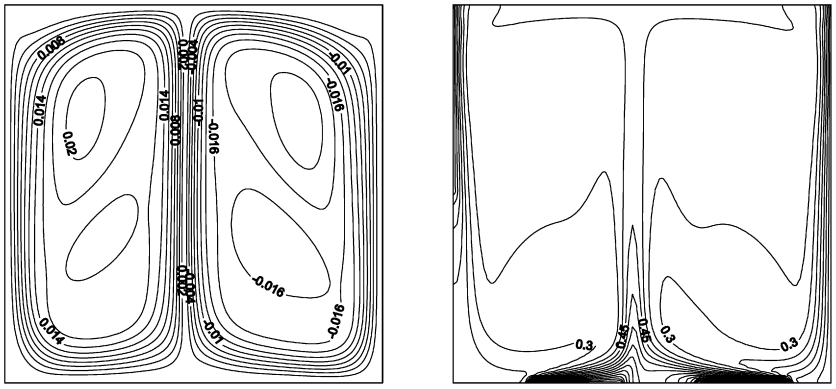

(a) θ_1=0.0, θ_2=1.0

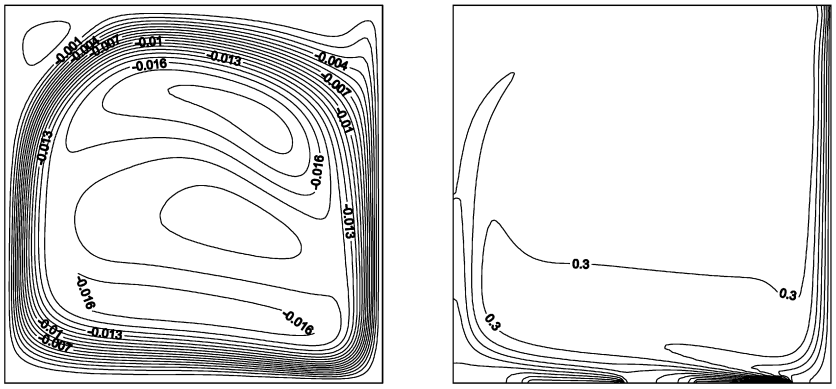

(b) θ_1=0.3, θ_2=0.7

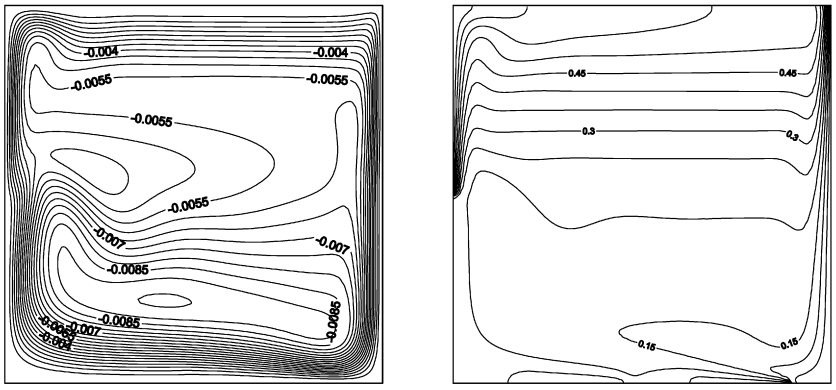

(c) θ_1=0.7, θ_2=0.3

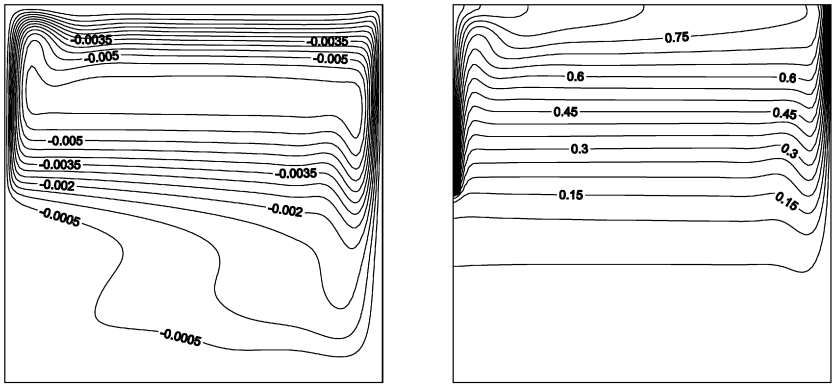

(d) θ_1=1.0, θ_2=0.0

Fig. 7. The streamlines and isothermal lines for different heating strengths at $Ra = 10^7$ in Case A.

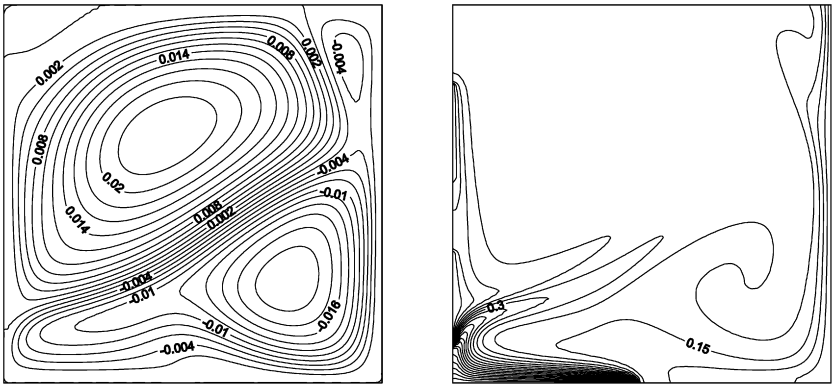

(a) θ_1=0.0, θ_2=1.0

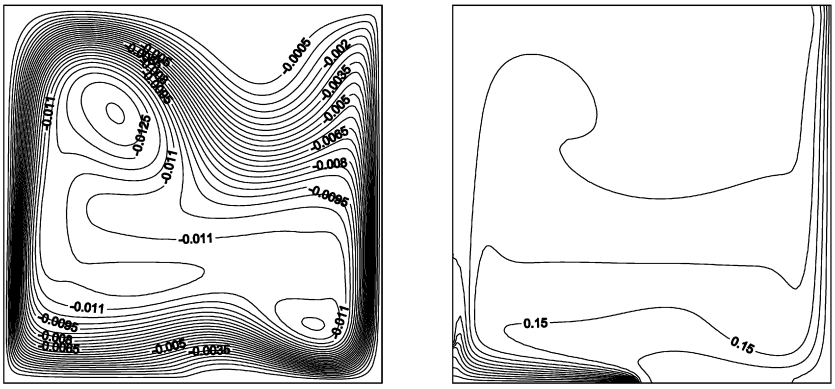

(b) θ_1=0.3, θ_2=0.7

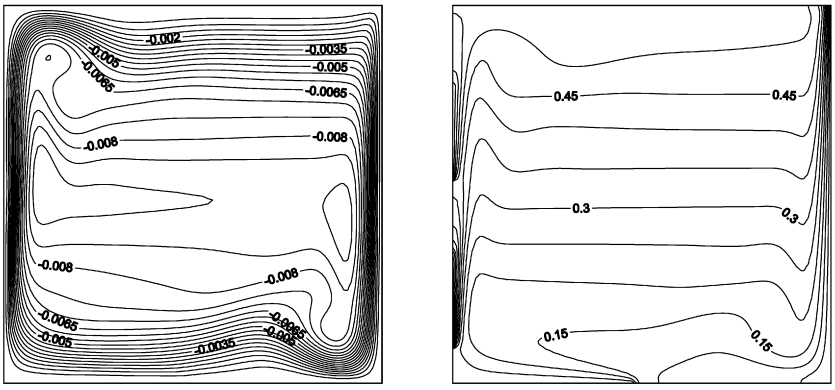

(c) θ_1=0.7, θ_2=0.3

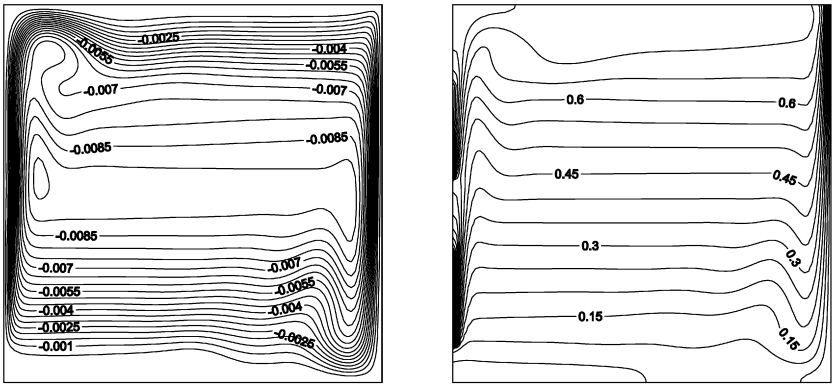

(d) θ_1=1.0, θ_2=0.0

Fig. 8. The streamlines and isothermal lines for different heating lengths at $Ra = 10^7$ in Case B.

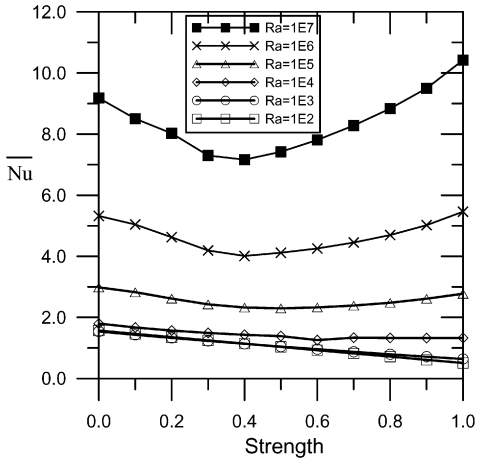

(a)

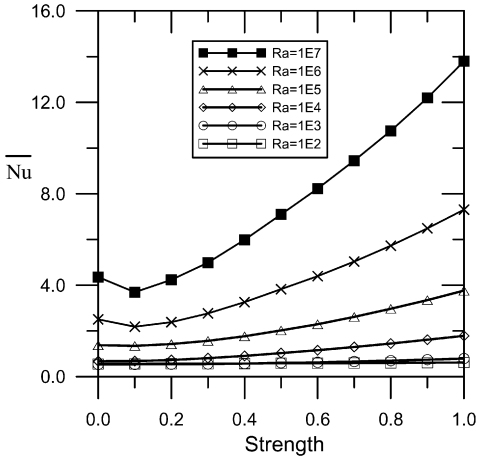

(b)

Fig. 9. (a) The effect of thermal strength θ_1 on average Nusselt numbers for Case A. (b) The effect of thermal strength θ_1 on average Nusselt numbers for Case B.

heat transfer rate on the left cold wall, thus appearing a low heat transfer rate on the right wall at $\theta_1 = 0$.

Gradually increasing the heat strength θ_1 on the side wall, which is equivalent to decrease the strength of heat source θ_2 on floor, causes different flow patterns in the core region as illustrated Figs. 7(b) and 8(b) for Cases A and B. In Case A, at $\theta_1 = 0.3$, the center of left cell drifts up and its size becomes smaller. However, the other cell evolves to different multi-cell patterns in the core region in which the tertiary eddy is observed. Further continuously increasing the heat strength on the left wall causes the left cell disappear and moves the upper eddy inside the main cell upwards. It is found that the thermal boundary layer is developing as shown in Fig. 7(c). As the heat strength advances to $\theta_1 = 1$ on the left wall, the roll center moves further upwards and the other cells were disappeared. The thermal boundary layer along the right wall has been developed. Accordingly, the corresponding heat transfer rate by increasing the thermal strength drops first, reaches its minimum value, and then progressively increases as shown in Fig. 9(a) for Case A. Moreover, it is seen that similar trend of heat transfer rate varying with θ_1 is consistently observed for Rayleigh number greater than 10^4 in Case A while the heat transfer rate is continuously decreased with the increase of heating strength for Rayleigh number below 10^4.

In Case B, the center of recirculation moves upwards as the vertical heat sources were heated up. Because the left roll is lifted and shrunk, which is not shown in the figure, the heat transfer is decreased at the corresponding heat strength $\theta_1 = 0.1$. It is especially notable that the rolling cell dies away and the appearance of a secondary eddy within the main cell was observed as the heating strength θ_1 is gradually increased to 0.3. This shows a distinguishing buoyancy influence on the thermal field and results in an apparent increase of heat transfer rate as shown in Fig. 9(b). In the extreme case of $\theta_1 = 1.0$, the thermal field indicates much more buoyancy effect and thermal boundary layers have been developed along the left and right walls. Comparing to the same condition in Case A, we find that the buoyancy induced flow in Case B is stronger than Case A. Consequently, the heat transfer rate in Case B is greater than Case A, which is manifested in Figs. 9(a) and 9(b). This suggests that placing heat sources on bottom wall with intensified thermal strengths can enhance a substantial heat transfer rate. Numerical values of average Nusselt number versus thermal strength θ_1 are depicted in Fig. 9(b) for different Rayleigh numbers.

5.3. Effect of heating length

In studying the heating length effect, computations are carried out for a range of Rayleigh numbers from 10^2 to 10^7 by allowing the variation of heating lengths. In Case A, the lateral heating size is varied from 0 to 1 and the longitudinal space and heating size are kept constant, i.e., $\ell_2 = 0.25$. At the same time, the heating strength is fixed by assigning $\theta_1 = 0.5$ and $\theta_2 = 0.5$. In Case B, the lateral space and heating size are kept constant ($\ell_1 = 0.25$) and the longitudinal heating size is varied from 0 to 1 in Case B with the heating strengths $\theta_1 = 0.5$ and $\theta_2 = 0.5$. The size effects of the single heat source on the left bottom wall or upper left wall on the thermal and fluid fields are shown in Figs. 10(a)–(d) and 11(a)–(d) plotted with streamlines and isothermal lines at $Ra = 10^7$, respectively. These figures indicate that the convection aggressively stratifies the temperature contours due to the increased heat source segment. Figs. 12(a) and 12(b) show the variation of average Nusselt number with the heater size for different Rayleigh numbers for Cases A and B. From Figs. 12(a) and 12(b), it is observed that for all Rayleigh numbers the heat transfer rates in terms of average Nusselt number gradually increase with increasing the heater size for Cases A and B. In the limit $\ell_2 = 1.0$ in Case B, the entire bottom wall was specified with uniform temperature boundary condition. This leads to more condensed temperature lines near the right bottom corner as shown in Fig. 11(d), reflecting a higher average Nusselt number at this extreme condition in Fig. 12(b).

6. Conclusion

To overcome the numerical difficulty associated with QUICK scheme in simulating high Rayleigh number cavity

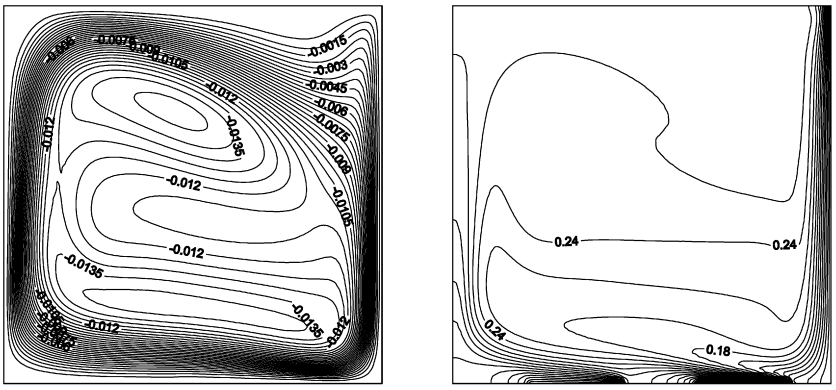

(a) ℓ_1=0.0, ℓ_2=0.25

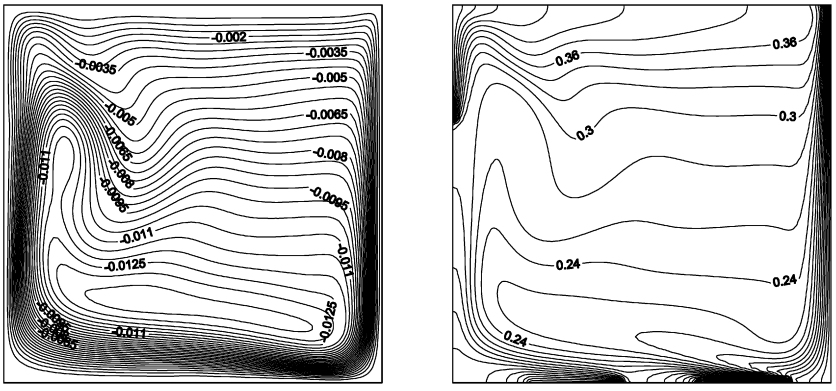

(b) ℓ_1=0.3, ℓ_2=0.25

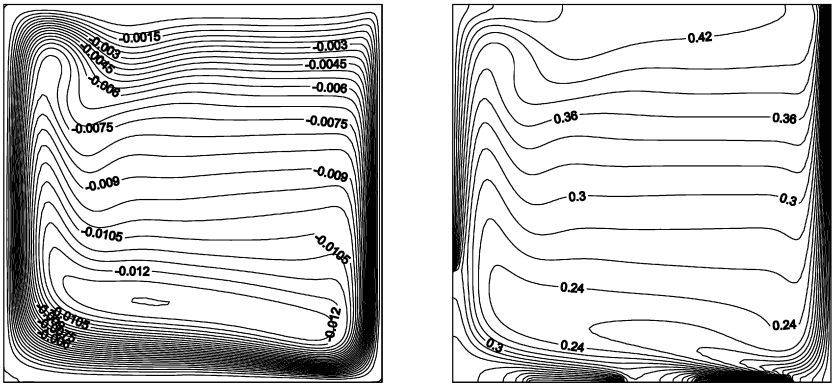

(c) ℓ_1=0.7, ℓ_2=0.25

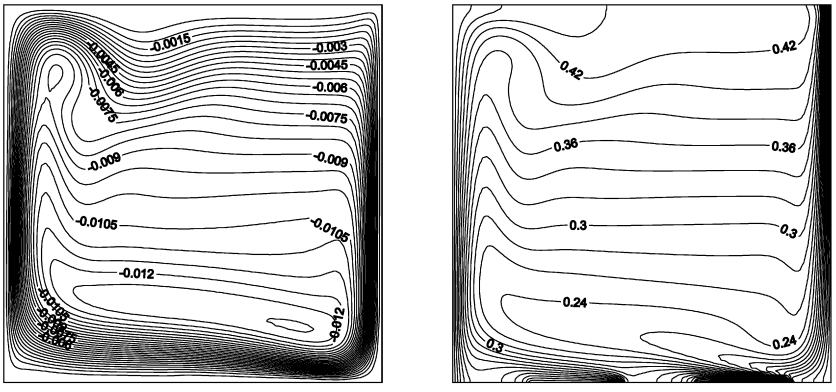

(d) ℓ_1=1.0, ℓ_2=0.25

Fig. 10. The streamlines and isothermal lines for different heating lengths at $Ra = 10^7$ in Case A.

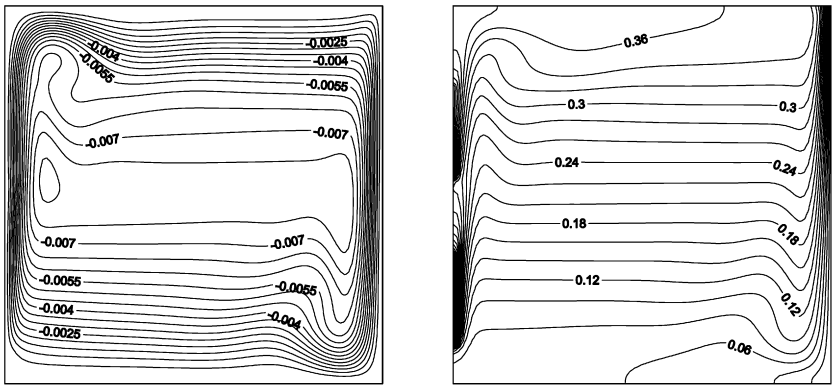

(a) ℓ_1=0.25, ℓ_2=0.0

(b) ℓ_1=0.25, ℓ_2=0.3

(c) ℓ_1=0.25, ℓ_2=0.7

(d) ℓ_1=0.25, ℓ_2=1.0

Fig. 11. The streamlines and isothermal lines for different heating lengths at $Ra = 10^7$ in Case B.

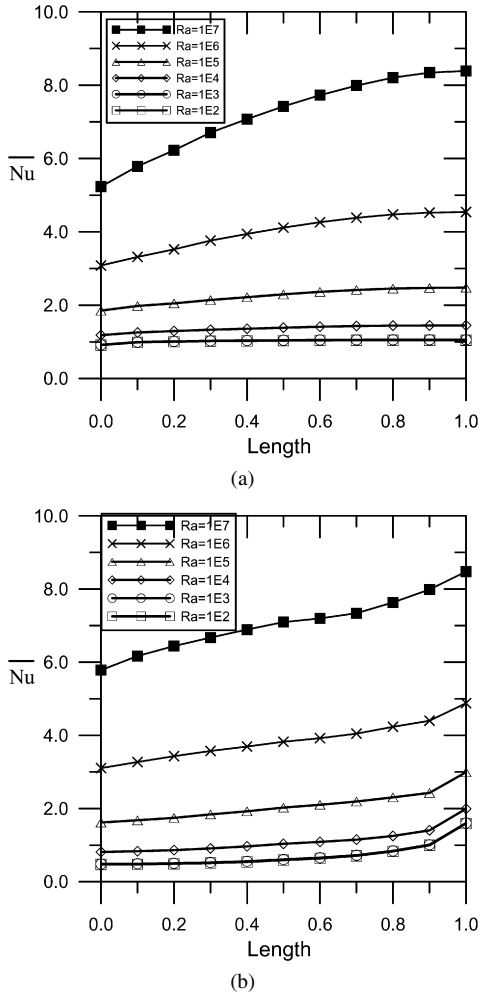

Fig. 12. (a) The effect of thermal length on average Nusselt numbers for Case A. (b) The effect of thermal length on average Nusselt numbers for Case B.

flow, the TOE scheme is proposed to resolve the numerical oscillation. Numerical investigation of natural convection in an enclosure with discrete heat sources on the bottom and lateral walls was completely executed for a range of Rayleigh numbers from 10^2 to 10^7 (total of 252 cases). By increasing Rayleigh number, an increasing average Nusselt number is observed for Cases A and B. However, Case A exhibits higher heat transfer rate compared with Case B. For Case A, by increasing the heating strength, it is found that the average Nusselt number decreases, attains its minimum, and increases as thermal strength increases. For Case B, it is seen that the average Nusselt number decreases at low heating strength ($\theta_1 = 0.1$) and then monotonically increases as thermal strength increases. This suggests that placing heat sources on bottom wall with intensified thermal strengths can enhance a substantial heat transfer rate from the numerical result in Case B. By increasing the length of heat source segment, the heat transfer rates in terms of average Nusselt number progressively increase with the increase of heating length for Cases A and B.

References

[1] H.H.-S. Chu, S.W. Churchill, C.V.S. Patterson, The effect of heater size, location, aspect ratio, and boundary conditions on two-dimensional, laminar, natural convection in rectangular channels, ASME J. Heat Transfer 98 (1976) 194–201.

[2] G.R. Ahmed, W.M. Yovanovich, Numerical study of natural convection from discrete heat sources in a vertical square enclosure, J. Thermophysics Heat Transfer 6 (1992) 121–127.

[3] O. Aydin, W.J. Yang, Natural convection in enclosures with localized heating flow below and symmetrical cooling from sides, Int. J. Numer. Methods Heat Fluid Flow 10 (2000) 518–529.

[4] M. Hasnaoui, E. Bilgen, P. Vasseur, Natural convection heat transfer in rectangular cavities partially heated from below, J. Thermophysics Heat Transfer 6 (1992) 255–264.

[5] Q.H. Deng, G.F. Tang, Y. Li, M.Y. Ha, Interaction between discrete heat sources in horizontal natural convection enclosures, Int. J. Heat Mass Transfer 45 (2002) 5117–5132.

[6] J.H. Bae, J.M. Hyun, Time-dependent buoyant convection in an enclosure with discret heat sources, Int. J. Thermal Sci. 43 (2004) 3–11.

[7] Q.H. Deng, G.F. Tang, Y. Li, A combined temperature scale for analyzing natural convection in rectangular enclosures with discret wall heat source, Int. J. Heat Mass Transfer 45 (2002) 3437–3446.

[8] G. De Felice, F.M. Denaro, C. Meola, Multidimensional single-step vector upwind schemes for highly convective transport problems, Numer. Heat Transfer, Part B 23 (1993) 425–460.

[9] B.P. Leonard, A stable and accurate convective modelling procedure based on quadratic upstream interpolation, Comput. Methods Appl. Mech. Engrg. 19 (1979) 59–98.

[10] P.H. Gaskell, A.K.C. Lau, Curvature-compensated convective transport: SMART, a new boundedness-preserving transport algorithm, Int. J. Numer. Methods Fluids 8 (1988) 617–641.

[11] G. De Vahl Davis, Natural convection of air in a square cavity: a benchmark numerical solution, Int. J. Numer. Methods Fluids 3 (1983) 249–264.